

The Mean Wind and Potential Temperature Flux Profiles in Convective Boundary Layers

LUOQIN LIU^{a,b}, SRINIDHI N. GADDE^b, AND RICHARD J. A. M. STEVENS^b

^a *Department of Modern Mechanics, University of Science and Technology of China, Hefei, Anhui, China*

^b *Physics of Fluids Group, Max Planck Center Twente for Complex Fluid Dynamics, J. M. Burgers Center for Fluid Dynamics, University of Twente, Enschede, Netherlands*

(Manuscript received 19 July 2022, in final form 17 April 2023, accepted 30 April 2023)

ABSTRACT: We develop innovative analytical expressions for the mean wind and potential temperature flux profiles in convective boundary layers (CBLs). CBLs are frequently observed during daytime as Earth's surface is warmed by solar radiation. Therefore, their modeling is relevant for weather forecasting, climate modeling, and wind energy applications. For CBLs in the convective-roll-dominated regime, the mean velocity and potential temperature in the bulk region of the mixed layer are approximately uniform. We propose an analytical expression for the normalized potential temperature flux profile as a function of height, using a perturbation method approach in which we employ the horizontally homogeneous and quasi-stationary characteristics of the surface and inversion layers. The velocity profile in the mixed layer and the entrainment zone is constructed based on insights obtained from the proposed potential temperature flux profile and the convective logarithmic friction law. Combining this with the well-known Monin–Obukhov similarity theory allows us to capture the velocity profile over the entire boundary layer height. The proposed profiles agree excellently with large-eddy simulation results over the range of $-L/z_0 \in [3.6 \times 10^2, 0.7 \times 10^3]$, where L is the Obukhov length and z_0 is the roughness length.

KEYWORDS: Atmosphere; Boundary layer; Convective parameterization; Idealized models; Large eddy simulations

1. Introduction

Convective boundary layers (CBLs) are frequently observed during daytime as Earth's surface is warmed by solar radiation (Stull 1988). Due to their frequent occurrence, the fundamental understanding of CBLs is highly relevant to agriculture, architectural design, aviation, climate modeling, weather prediction, and wind energy applications, to name a few. The modern scientific literature on CBLs goes back over 100 years. Initially, the focus was on low-altitude measurements, and with the introduction of more advanced measurement techniques, the focus gradually shifted upward. However, only after the introduction of large-eddy simulations (LES) in the early 1970s, it has become widely accepted that thermodynamic indicators are most suitable to identify the different CBL regions (LeMone et al. 2019). However, obtaining analytical profiles that describe the wind and potential temperature flux in the entire CBL has remained challenging due to the different flow physics in the various CBL regions.

The CBL can be subdivided into three layers (excluding the roughness sublayer), i.e., the surface layer, the mixed layer, and the entrainment zone (see Fig. 1). The surface layer is characterized by a superadiabatic potential temperature gradient and a strong wind shear, which is usually described by the Monin–Obukhov similarity theory (MOST; Monin and Obukhov 1954). According to the MOST the nondimensional wind speed and potential temperature gradient profiles are universal functions of the dimensionless height z/L , where z is the height above the surface and L is the surface Obukhov

length (Obukhov 1946; Monin and Obukhov 1954). Many studies have pointed out that the MOST does not explain all important surface-layer statistics under convective conditions (Panofsky et al. 1977; Khanna and Brasseur 1997; Johansson et al. 2001; McNaughton et al. 2007; Salesky and Anderson 2020; Cheng et al. 2021) or very stable conditions (Mahrt 1998; Cheng et al. 2005). In particular, the normalized wind gradient $\phi_m = (\kappa z/u_*) (\partial U / \partial z)$ depends both on z/L and z_i/L (Khanna and Brasseur 1997; Johansson et al. 2001), where z_i is the height of the inversion layer (see Fig. 1). Nevertheless, MOST is still widely used in numerical weather prediction and climate models (Salesky and Anderson 2020), and thus will be used in the theoretical analysis and numerical simulations of this study. MOST applies only to the surface layer, and for it to be applicable, the absolute value of the Obukhov length L must be smaller than the height of the surface layer. Therefore, we only consider the CBL with $-z_i/L \gg 1$. In particular, we focus on the convective-roll dominant regime with $-z_i/L \gtrsim 10$ (Salesky et al. 2017). Furthermore, we focus on dry and cloud-free CBLs to avoid complications due to physical processes like evaporation, precipitation, and cloud formation.

The mixed layer is characterized by intense vertical mixing caused by warm air thermals rising from the ground. Within the mixed layer, the magnitude of the mean velocity is much larger than the variations in the mean velocity. Thus, for applications where the mean velocity gradient is unimportant, the wind speed and potential temperature can be regarded as uniform (Kaimal et al. 1976; Salesky et al. 2017). This insight is incorporated in various CBL models (Lilly 1968; Deardorff 1973; Stull 1976; Deardorff 1979; Tennekes and Driedonks 1981; Garratt et al. 1982). The entrainment zone is characterized by entrainment of air from the free atmosphere. Deardorff et al. (1980)

Corresponding author: Luoqin Liu, luoqinliu@ustc.edu.cn

DOI: 10.1175/JAS-D-22-0159.1

© 2023 American Meteorological Society. This published article is licensed under the terms of the default AMS reuse license. For information regarding reuse of this content and general copyright information, consult the AMS Copyright Policy (www.ametsoc.org/PUBSReuseLicenses).

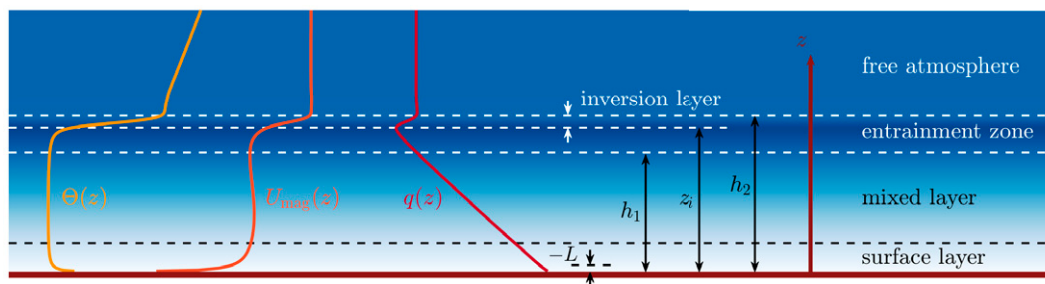


FIG. 1. Profiles of the potential temperature Θ , wind speed U_{mag} , and potential temperature flux q in the CBL. The vertical lines with double arrows indicate different length scales in the CBL, namely, from left to right, the Obukhov length L , the lowest height where the potential temperature flux first reaches zero, h_1 , the inversion-layer height at which the potential temperature flux reaches its minimum value, z_i , and the height where the potential temperature flux first recovers zero, h_2 . The background color indicates the magnitude of the potential temperature flux $q(z)$ for case 2; see Table 1.

found in laboratory experiments that the ratio of the entrainment zone thickness to the depth of the mixing layer decreases asymptotically with increasing Richardson number Ri as follows ($h_2 - h_1/h_1 = 0.21 + 1.31/Ri$) (see Fig. 1 for the definitions of h_1 and h_2). This ratio is essential for developing entrainment models and has been studied extensively (Lilly 1968; Sullivan et al. 1998; Zilitinkevich et al. 2012; Haghsheenas and Mellado 2019). The potential temperature flux profile decreases linearly with height and becomes negative in the entrainment zone. The entrainment flux ratio Π_m , which is defined as the ratio of the potential temperature flux at the inversion-layer height to its value at the ground, turns out to be nearly constant, i.e., $\Pi_m \approx -0.2$ (Stull 1976; Sorbjan 1996; Conzemius and Fedorovich 2006; Sun and Wang 2008; LeMone et al. 2019). Note that the inversion layer is the upper region of the entrainment zone in which the potential temperature flux increases steeply from its minimum value at $z = z_i$ to zero at $z = h_2$ (see Fig. 1).

The geostrophic wind (U_g, V_g) and the friction velocity u_* are usually connected through the well-known geostrophic drag law, which was initially derived for neutral boundary layers (Rossby and Montgomery 1935; Blackadar and Tennekes 1968; Tennekes and Lumley 1972) and later extended to include buoyancy effects (Zilitinkevich 1969). To include the effect of unsteadiness, Zilitinkevich and Deardorff (1974) and Arya (1975) proposed to replace the Ekman depth $u_*/|f|$ in the geostrophic drag law, where f is the Coriolis parameter, with the time-dependent inversion-layer height z_i . However, significant disparities were observed between the geostrophic drag law for CBLs and measurement data (Zilitinkevich 1975). Garratt et al. (1982) derived a relationship for the velocity defects in the mixed layer using a three-layer CBL model, which accounts for the effects of entrainment, baroclinity, advection, and local acceleration. In their formulation, the velocity defects are defined as the differences between the mixed-layer-averaged winds and the geostrophic winds. They proposed a geostrophic drag law to relate the geostrophic winds and the friction velocity based on the assumption that the mean velocity at the top of the surface layer is equal to that in the mixed layer. In addition, an empirical stability function ψ_m , which may be inaccurate for large values of $-z/L$, is employed.

Recently, Tong and Ding (2020) analytically derived the convective logarithmic friction law from first principles. They identified three scaling layers for the CBL with $-z_i/L \gg 1$: the outer layer, the inner-outer layer, and the inner-inner layer. The characteristic length scales for these three layers are the inversion-layer height z_i , the Obukhov length L , and the roughness length z_0 , respectively. The mixed-layer mean velocity scale U_m and the geostrophic wind component V_g are the characteristic streamwise and spanwise velocity scales in the outer layer. The difference between the horizontally and temporally averaged velocity $U(z)$ and U_m is the mixed-layer velocity-defect law, which has a velocity scale of $u_*^2/w_* \ll U_m$, with w_* the convective velocity. This indicates that U_m is very close to the mean velocity $U(z)$ in the mixed layer. For the inner-outer layer they derived the surface-layer velocity-defect law, which states that the velocity defect $U - U_m$ scales with u_* . The convective logarithmic friction law is derived from matching the law of the wall in the inner-inner layer with the velocity-defect law in the surface layer. This exact leading-order result relates the friction velocity (u_*) to the mixed-layer velocity scale (U_m). The difference between U_g and U_m scales as $(u_*^2 w_e)/(f z_i)^2$, where w_e is the entrainment velocity and V_g scales as $-u_*^2/(f z_i)$. Thus, up to nondimensional coefficients, one can relate the geostrophic velocities (U_g, V_g) to u_* . As Tong and Ding (2020) do not consider the effects of the entrainment zone the velocity profiles are only valid for $z/z_i < 0.4$.

Various time-dependent models have been developed to explicitly account for entrainment processes at the top of CBLs (Troen and Mahrt 1986; Noh et al. 2003; Hong et al. 2006). For example, the countergradient transport method (Holtslag and Moeng 1991) and the eddy-diffusivity mass-flux approach (Siebesma et al. 2007; Li et al. 2021) are widely used in coarse-resolution climate models. In general, the potential temperature is time dependent (Lilly 1968) and the entrainment velocity can affect the mean wind speed in the mixed layer (Tong and Ding 2020). However, the velocity and potential temperature flux profiles are quasi stationary, and therefore, similarity theory can be employed to obtain analytical expressions for these profiles shapes (Zilitinkevich and Deardorff 1974; Arya 1975; Zilitinkevich et al. 1992).

In this study, we focus on the derivation of analytical expressions for the mean velocity and potential temperature flux profiles in cloud-free CBLs. We use a perturbation method approach to construct an analytical expression for the normalized potential temperature flux profile as a function of height, taking into account the characteristics of both the surface layer and the capping inversion layer. The depth of the entrainment zone is connected to the convective logarithmic friction law to obtain analytical expressions for the velocity profile in the mixed layer and the entrainment zone. As remarked previously, the surface layer is still described by the MOST.

The organization of the paper is as follows. In [section 2](#) we obtain analytical expression for the potential temperature flux and wind profiles. In [section 3](#) we validate the proposed profiles against LES. The conclusions are given in [section 4](#).

2. Theory

a. Potential temperature flux profile

The potential temperature flux profile provides a precise and convenient demarcation between the mixed layer and the entrainment zone of the CBL ([Deardorff 1979](#); [Deardorff et al. 1980](#)). [Figure 1](#) shows a definition of the various length scales in the CBL. Previous studies ([Kaimal et al. 1976](#); [Deardorff et al. 1980](#); [Moeng and Sullivan 1994](#); [Noh et al. 2003](#); [Garcia and Mellado 2014](#); [Haghsheenas and Mellado 2019](#)) showed that the potential temperature flux (including both the turbulent part and the diffusive part) in CBLs decreases linearly from its maximum value at the surface to a minimum value at $z = z_i$, and then increases steeply to zero in a narrow region $z_i \leq z \leq h_2$ at the top of the boundary layer ([Fig. 1](#)). For typical CBLs the condition $|dz_i/dt| \ll w_*$ holds, which implies that the boundary layer is quasi stationary ([Nieuwstadt et al. 2016](#), section 7.6). Besides, the potential temperature flux q is fixed at the surface, and its value at the inversion-layer height is nearly a constant fraction of the value at the ground q_w . Therefore, the normalized potential temperature flux $q(z, t)/q_w$ only depends on the similarity variable $\xi = z/h_2(t)$, i.e.,

$$q(z, t)/q_w = \Pi(\xi), \quad (1)$$

where the form of Π remains to be determined. Using the potential temperature equation, we derive below an ordinary differential equation (ODE) for the determination of Π . However, it is important to emphasize that this does not mean Π is independent of time as the similarity variable $\xi = z/h_2(t)$ is still time dependent.

Under the assumption of horizontal homogeneity, the potential temperature equation reduces to

$$\frac{\partial \Theta}{\partial t} = -\frac{\partial q}{\partial z} = -\frac{q_w}{h_2} \Pi', \quad (2)$$

where $\Pi' = \partial \Pi / \partial \xi$. In the mixed layer the potential temperature Θ is almost spatially uniform and hence the left-hand side of [Eq. \(2\)](#) is independent of z . Therefore, the governing

equation of the potential temperature flux in the mixed layer can be approximated as

$$-\Pi' = c_{\Pi}, \quad (3)$$

where c_{Π} is the gradient of the normalized potential temperature flux in the mixed layer (see [Fig. 1](#)). In the mixed layer, it is well-known that the eddy-diffusivity approach cannot adequately describe the potential temperature flux as the gradient of the potential temperature nearly vanishes ([Wyngaard 2010](#)). In contrast, in the inversion layer the potential temperature gradient is dominant such that the potential temperature flux can be approximated by $q = -v_{\theta} \partial \Theta / \partial z$. Here $v_{\theta} \propto |w_e|(h_2 - z_i)$ is the eddy diffusivity and $w_e = dz_i/dt$ is the entrainment velocity. That the ratio h_2/z_i is approximately constant implies that $\partial \xi / \partial t = -(z/h_2^2)(h_2/z_i)(dz_i/dt) \approx -w_e/z_i$. From the zero-order jump model dz_i^2/dt is independent of time ([Nieuwstadt et al. 2016](#), section 7.6), such that v_{θ} is approximately constant. Then, by taking the vertical derivative of [Eq. \(2\)](#), we obtain that

$$\epsilon \Pi'' - \Pi' = 0, \quad (4)$$

where ϵ is a small dimensionless parameter,

$$\epsilon \equiv c \frac{h_2 - z_i}{h_2} \ll 1, \quad (5)$$

with $c = (v_{\theta} z_i) / [-w_e h_2 (h_2 - z_i)] = 1/2$ being an empirical constant that is determined by comparing the model profiles to the simulation results. This indicates that the parameter ϵ represents the half thickness of the inversion layer normalized by the boundary layer depth (see [Fig. 1](#)). To get the potential temperature flux profile in the entire boundary layer, we combine [Eqs. \(3\) and \(4\)](#), which leads to the following second-order ODE for the potential temperature flux,

$$\epsilon \Pi'' - \Pi' = c_{\Pi}, \quad \Pi(0) = 1, \quad \Pi(1) = 0. \quad (6)$$

The solution of [Eq. \(6\)](#) reads

$$\Pi = 1 - c_{\Pi} \xi + (c_{\Pi} - 1) \frac{e^{\xi/\epsilon} - 1}{e^{1/\epsilon} - 1}, \quad 0 \leq \xi \leq 1. \quad (7)$$

Since $\epsilon \ll 1$, the value of Π in the bulk of the mixed layer can be approximated as

$$\Pi \approx 1 - c_{\Pi} \xi. \quad (8)$$

Similarly, since $\Pi = 0$ at $\xi = h_1/h_2$, the slope c_{Π} reduces to

$$c_{\Pi} = h_2/h_1 > 1. \quad (9)$$

Therefore, the ratio of the entrainment zone thickness to the mixing-layer depth is

$$R \equiv (h_2 - h_1)/h_1 = c_{\Pi} - 1 > 0. \quad (10)$$

[Deardorff et al. \(1980\)](#) found in laboratory experiments that the value of R is between 0.2 and 0.4. Furthermore, the

entrainment flux ratio Π_m , i.e., the minimum value of Π , can be approximated as

$$\Pi_m \approx 1 - c_{\Pi}(1 - 2\epsilon) \approx -(R - 2\epsilon). \quad (11)$$

Stull (1976) and Sorbjan (1996) found that $-0.3 \leq \Pi_m \leq -0.1$. These results are consistent with the LES results of Sullivan and Patton (2011) with $\Pi_m \approx -0.2$, the empirical results of Lenschow (1974) with $\Pi_m = -0.1$, and the direct numerical simulation results of Garcia and Mellado (2014) with $\Pi_m \approx -0.12$.

We note that the perturbation method approach to model the potential temperature flux profile was recently introduced by Liu et al. (2021b) for conventionally neutral atmospheric boundary layers where the surface potential temperature flux is always zero. However, it should be noted that in the CBLs under consideration, the surface is heated and thermal plumes are generated at the ground, resulting in significantly different turbulence generation mechanisms. The applicability of the perturbation method approach to model the strong inversion layer relies on its ability to capture the strong gradients in the inversion layer. Here we used the second-order ODE defined by Eq. (6) to model the potential temperature flux profile as our a posteriori tests confirm that this is sufficient to capture the inversion layer accurately. Higher-order terms could be incorporated, but this is not considered here to keep the obtained profiles relatively simple. An important observation is that the perturbation method approach is consistent with the finding of Garcia and Mellado (2014). They showed that the vertical structure of the entrainment zone is best described by two overlapping sublayers characterized by different length scales, namely, the mean penetration depth of an overshooting thermal for the upper sublayer and the thickness of the CBL for the lower sublayer. Similarly, the second-order ODE, i.e., Eq. (6), indicates that there are two distinct length scales for the description of the entrainment zone (Fig. 1): one is the upper sublayer with $z_i \leq z \leq h_2$, where the gradient of potential temperature flux is proportional to $-(q_w \Pi_m)/(2\epsilon h_2)$, and the other is the lower sublayer with $h_1 \leq z \leq z_i$, where the gradient of potential temperature flux is proportional to $(q_w \Pi_m)/z_i$. Since $\epsilon \ll 1$ the potential temperature flux varies more steeply in the upper sublayer than in the lower sublayer.

b. Wind profile

We consider MOST to describe the wind speed profile in the surface layer (Monin and Obukhov 1954). In surface-layer coordinates, it states that the nondimensional streamwise velocity gradient can be written as

$$\frac{\kappa z}{u_*} \frac{dU}{dz} = \phi_m \left(\frac{z}{L} \right), \quad (12)$$

where ϕ_m is the dimensionless stability correction function and $L = -u_*^3/(\kappa \beta q_w)$ is the Obukhov length with β the buoyancy parameter. By integrating Eq. (12), one can obtain the explicit formula for the streamwise velocity U ,

$$\frac{\kappa U}{u_*} = \ln \left(\frac{z}{z_0} \right) - \psi_m \left(\frac{z}{L} \right). \quad (13)$$

Here $\kappa = 0.4$ is the von Kármán constant, z_0 is the roughness length, and

$$\psi_m = \int_{z_0/L}^{z/L} \frac{1 - \phi_m(\xi)}{\xi} d\xi \quad (14)$$

is the stability correction function for the momentum. We use the well-known Businger–Dyer expression (Paulson 1970; Businger et al. 1971; Dyer 1974; Brutsaert 1982)

$$\psi_m = \ln \frac{(1+x^2)(1+x)^2}{8} - 2 \arctan x + \frac{\pi}{2}, \quad (15)$$

with $x = (1 - 16z/L)^{1/4}$ to model the stability correction function, but we note that other parameterizations exist (Katul et al. 2011). Note that $\psi_m = 0$ for $x = 1$ (or $L = \infty$), which reduces Eq. (13) to the classical logarithmic law for neutral boundary layers.

To model the wind profile U in the mixed layer and entrainment zone, we again employ a second-order ODE. In general, the detailed wind profile evolves when stability changes. However, the variations of the mean velocity are small compared to the magnitude of the mean velocity in the mixed layer when the stability parameter $-z_i/L \gtrsim 10$ (e.g., Salesky et al. 2017), which covers the range of stability conditions considered in this study. Thus, we can assume that the ODE is dominated by the $U' = 0$ term in most of the domain. Recently, Tong and Ding (2020) derived the convective logarithmic friction law from first principles, which connects the mixed-layer mean velocity scale U_m and the friction velocity u_* in the convective-roll dominant regime ($-z_i/L \gg 1$) as follows,

$$\frac{U_m}{u_*} = \frac{1}{\kappa} \ln \left(-\frac{L}{z_0} \right) - C, \quad (16)$$

where $C = 1$ is an empirical constant determined from our LES database (see below).

From the potential temperature flux profile modeling we learned that the ODE should have a second-order derivative term $\epsilon U''$ to model the entrainment zone near the top of the boundary layer. The top boundary condition is given by the geostrophic wind component U_g . The lower boundary condition is given by equaling Eqs. (13) and (16), namely, $U(\xi_0) = U_m$, since Tong and Ding (2020) showed that U_m is very close to $U(z)$ in the mixed layer. Here ξ_0 represents the height of the top of surface layer, which can be determined using Eqs. (13) and (16),

$$\ln \left(-\frac{h_2}{L} \xi_0 \right) - \psi_m \left(\frac{h_2}{L} \xi_0 \right) = -\kappa C \Rightarrow \xi_0 = \xi_0 \left(\frac{h_2}{L} \right). \quad (17)$$

Because $\epsilon \ll 1$, the solution obtained from $U(\xi_0) = U_m$ is almost the same as from $U(0) = U_m$, while the expression of the latter is much simpler. Therefore, we model the profile of the streamwise velocity U in the mixed layer and the entrainment zone as

$$\epsilon U'' - U'' = 0, \quad U(0) = U_m, \quad U(1) = U_g. \quad (18)$$

TABLE 1. Summary of all simulated cases. Here $\Gamma = \partial\Theta/\partial z$ is the vertical derivative of the mean potential temperature in the free atmosphere, q_w is the surface potential temperature flux, z_0 is the roughness length, u_* is the friction velocity, U_m is the wind speed in the mixed layer, L is the Obukhov length, z_i is the inversion-layer height, $|V_g|$ is the magnitude of the spanwise geostrophic wind, ϵ and c_{II} are dimensionless parameters calculated by Eqs. (5) and (9), respectively, and $Ri = \beta\Delta\Theta z_i/w_*^2$ is the Richardson number, where $\Delta\Theta = \Theta(h_2) - \Theta(h_1)$ is the potential temperature difference across the entrainment zone and $w_* = (\beta q_w z_i)^{1/3}$ is the convective velocity.

Case	Γ (K km ⁻¹)	q_w (K m s ⁻¹)	z_0 (m)	u_* (m s ⁻¹)	U_m (m s ⁻¹)	$ V_g $ (m s ⁻¹)	ϵ	c_{II}	Ri	$-z/L$	$-L/z_0$
1	9	0.24	0.16	0.562	7.60	2.00	0.044	1.32	56.1	19.2	3.6×10^2
2	3	0.24	0.16	0.563	7.59	1.87	0.052	1.34	51.0	19.1	3.6×10^2
3	1	0.24	0.16	0.562	7.59	1.84	0.055	1.34	47.9	19.2	3.6×10^2
4	3	0.12	0.16	0.533	7.70	2.20	0.046	1.34	94.2	11.0	0.6×10^3
5	3	0.24	0.016	0.463	8.44	1.17	0.050	1.33	51.0	34.5	2.0×10^3
6	3	0.20	0.02	0.468	8.36	1.32	0.046	1.31	59.6	27.5	2.0×10^3
7	3	0.12	0.016	0.444	8.45	1.43	0.038	1.31	91.5	19.0	3.5×10^3
8	3	0.20	0.002	0.392	8.93	0.86	0.033	1.28	55.5	47.3	1.2×10^4
9	3	0.24	0.0016	0.389	8.94	0.75	0.044	1.30	50.4	58.3	1.2×10^4
10	3	0.12	0.0016	0.375	8.94	0.88	0.036	1.30	93.9	31.6	2.1×10^4
11	3	0.20	0.0002	0.334	9.24	0.57	0.041	1.30	58.6	75.8	0.7×10^5

The solution of Eq. (18) is

$$U = U_m + (U_g - U_m) \frac{e^{\xi/\epsilon} - 1}{e^{1/\epsilon} - 1}. \quad (19)$$

We note that Eq. (19) is only valid in the mixed layer and entrainment zone as the wind speed in the surface layer is still modeled using the MOST. By combining Eqs. (13) and (19) and recalling that Eq. (13) increases monotonically as z increases, we obtain the following analytic description of the streamwise velocity profile $U(z)$ for the entire CBL,

$$U = \begin{cases} \frac{u_*}{\kappa} \left[\ln\left(\frac{z}{z_0}\right) - \psi_m\left(\frac{z}{L}\right) \right], & \xi \leq \xi_0, \\ U_m + (U_g - U_m) \frac{e^{\xi/\epsilon} - 1}{e^{1/\epsilon} - 1}, & \xi_0 < \xi \leq 1, \end{cases} \quad (20)$$

where ξ_0 is given by Eq. (17). As remarked in section 1 the surface-layer profile contains two length scales, i.e., z_0 for the inner-inner layer and the Obukhov length L for the inner-outer layer. Similarly, the velocity profile for the mixed layer and entrainment zone contains two length scales, i.e., z_i to describe the mixed layer and $h_2 - z_i = 2\epsilon h_2$ to describe the upper sublayer of the entrainment zone. This confirms the view presented by Tong and Ding (2020) that the entrainment zone has a different scaling than the surface and mixed layers, and can therefore be considered as another inner layer in the overall CBL problem. We note that the proposed analytical profile is empirical, similar to the MOST, and that the parameter ϵ parameterizes the effect of various physical processes. We further note that U_m and u_* are related as given by Eq. (16), and that the difference $U_g - U_m$ scales as $(u_*^2 w_e)/(f z_i)^2$ (Tong and Ding 2020). Thus, Eq. (20) is predictive if the entrainment velocity w_e is given as an input parameter. To determine the value of w_e , one may need to revisit the entrainment processes at the top of CBLs (e.g., Garcia and Mellado 2014). In addition, the velocity predicted by Eq. (20)

is continuous throughout the boundary layer and applicable for the considered ranges (see Fig. 5 below). However, its first derivative is discontinuous at the patching location $\xi = \xi_0$. This is a typical character of low-order models (Garratt et al. 1982). To capture the smooth transition, a high-order model is needed (Tong and Ding 2020). We leave these for future work.

To model the wind profile V in the mixed layer and entrainment zone, we use a similar ODE as Eq. (18). The top boundary condition is given by the geostrophic wind component V_g . As the spanwise velocity V is small compared to the streamwise velocity U in the mixed layer (Tong and Ding 2020), the lower boundary condition is given by $V(\xi_0) = V(0) = 0$. Therefore, we model the profile of the spanwise velocity V in the entire boundary layer using

$$\epsilon V'' - V' = 0, \quad V(0) = 0, \quad V(1) = V_g. \quad (21)$$

The solution of Eq. (21) is

$$V = V_g \frac{e^{\xi/\epsilon} - 1}{e^{1/\epsilon} - 1}. \quad (22)$$

Since V_g scales as $-u_*^2/(f z_i)$ (e.g., Wyngaard 2010; Tong and Ding 2020), the geostrophic wind component V_g can be connected to u_* , up to a nondimensional coefficient $-V_g f z_i / u_*^2 = 0.66$, which is determined from our LES database (see Table 1).

3. Numerical validation

a. Numerical method and computational setup

We use LES to simulate the CBL flow over an infinite flat surface with homogeneous roughness. We integrate the spatially filtered Navier–Stokes equations and the filtered transport equation for the potential temperature (Albertson 1996; Albertson and Parlange 1999; Gadde et al. 2021; Liu et al. 2021a,b; Liu and Stevens 2021). Molecular viscosity is neglected as the Reynolds number in the atmospheric boundary layer flow

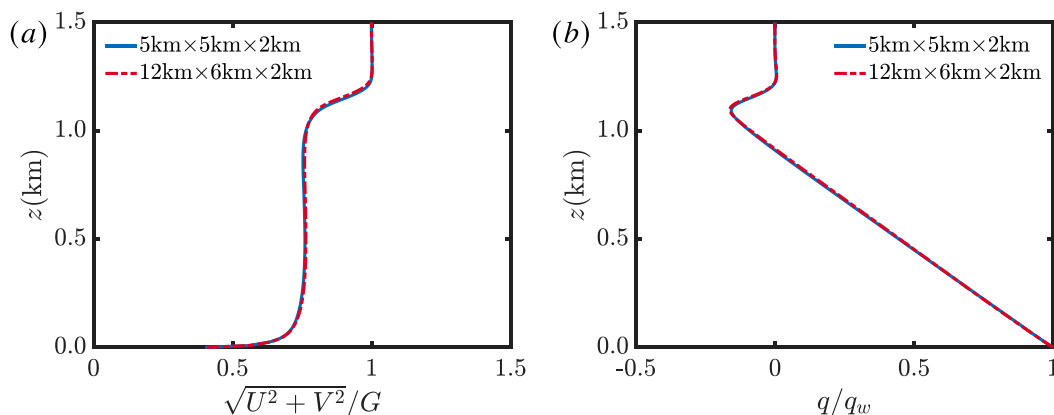


FIG. 2. The comparison of simulated (a) normalized wind speed $\sqrt{U^2 + V^2}/G$ and (b) normalized potential temperature flux q/q_w profiles for case 2 (see Table 1) with different computational domain sizes.

is very high, and we use the advanced Lagrangian-averaging scale-dependent model to parameterize the subgrid-scale shear stress and potential temperature flux (Bou-Zeid et al. 2005; Stoll and Porté-Agel 2008). We note that the Lagrangian-averaging scale-dependent model has been extensively validated and widely used in the literature (Bou-Zeid et al. 2005; Stoll and Porté-Agel 2008; Calaf et al. 2010; Wu and Porté-Agel 2011; Zhang et al. 2019; Gadde et al. 2021).

Our code is an updated version of the one used by Albertson and Parlange (1999). The grid points are uniformly distributed, and the computational planes for horizontal and vertical velocities are staggered in the vertical direction. The first vertical velocity grid plane is located at the ground. The first grid point for the horizontal velocity components and the potential temperature is located at half a grid distance above the ground. We use a second-order finite difference method in the vertical direction and a pseudospectral discretization in the horizontal directions. Time integration is performed using the second-order Adams–Bashforth method. The projection method is used to enforce the divergence-free condition. At the top boundary, we impose a constant potential temperature lapse rate, zero vertical velocity, and zero shear stress boundary condition. At the bottom boundary, we employ the classical wall stress and potential temperature flux formulations based on the MOST (Moeng 1984; Bou-Zeid et al. 2005; Stoll and Porté-Agel 2008; Gadde et al. 2021).

We perform 11 LES to verify the validity of the derived wind speed and potential temperature flux profiles for CBLs. The computational domain is $5\text{ km} \times 5\text{ km} \times 2\text{ km}$ and the grid resolution is $256 \times 256 \times 256$. Due to large computational expense, only several external parameters are varied in the simulations. The flow is driven by the geostrophic wind of $G = \sqrt{U_g^2 + V_g^2} = 10\text{ m s}^{-1}$, the buoyancy parameter is $\beta = 0.0325\text{ m (s}^2\text{ K)}^{-1}$, and the Coriolis parameter is $f = 1 \times 10^{-4}\text{ rad s}^{-1}$ (Moeng and Sullivan 1994; Abkar and Moin 2017; Gadde et al. 2021). To ensure the CBLs are in the convective-roll dominant regime with $-z_i/L \gtrsim 10$, the surface potential temperature flux is set to $q_w = 0.12\text{--}0.24\text{ K m s}^{-1}$. Note that the convective logarithmic friction law [Eq. (16)] is

derived very recently by Tong and Ding (2020) and tested only in a relatively narrow range of $-L/z_0$, namely, $-L/z_0 \in [2.5 \times 10^2, 1.5 \times 10^3]$. To evaluate the performance of this law in much wider range, i.e., $-L/z_0 \in [3.6 \times 10^2, 0.7 \times 10^5]$, the roughness length is varied between $z_0 = 0.0002\text{ m}$ and 0.16 m , where the lower bound of z_0 is set to a representative value of the sea surface (Wieringa et al. 2001). The vertical potential temperature gradient is varied between $\Gamma = 1$ and 9 K km^{-1} to capture the relevant range observed in atmospheric measurements (Sorbján 1996). The velocity field is initialized with the geostrophic wind $G = 10\text{ m s}^{-1}$. The initial potential temperature is 300 K up to 937 m and increases with 8 K in the next 126 m above. Above 1063 m the constant vertical derivative of the potential temperature Γ is specified. The simulations are run for about 25 large-eddy turnover times $T = z_i/w_*$, where $w_* = (\beta q_w z_i)^{1/3}$ is the convective velocity scale, and the statistics are computed from the time interval of $12T$ to $25T$ when the boundary layer is quasi stationary (Ding and Tong 2021). We note that inertial oscillation develops as the flow is initialized with a profile in geostrophic equilibrium (Schröter et al. 2013). However, it should have only negligible effect on the simulated statistics since the typical large-eddy turnover time $T \approx 10\text{ mins}$ is two orders smaller than the natural inertial periodicity $2\pi/f \approx 17.5\text{ h}$.

A summary of all simulated cases is presented in Table 1. Note that the cases in Table 1 are arranged such that the value of $-L/z_0$ increases monotonically. Furthermore, we note that case 2 has been validated against atmospheric observations, and the simulation results obtained using different subgrid-scale models and grid resolutions is very similar (Gadde et al. 2021). To show the simulated results are independent of the computational domain size, we have performed an additional simulation for case 2 in a larger computational domain ($12\text{ km} \times 6\text{ km} \times 2\text{ km}$) on a mesh with $600 \times 300 \times 240$ nodes such that the grid spacings are nearly identical. Figure 2 shows the simulated wind speed and potential temperature flux profiles for case 2. The good agreement between the results obtained with different computational domain size confirms that the simulated results are independent of the computational domain size.

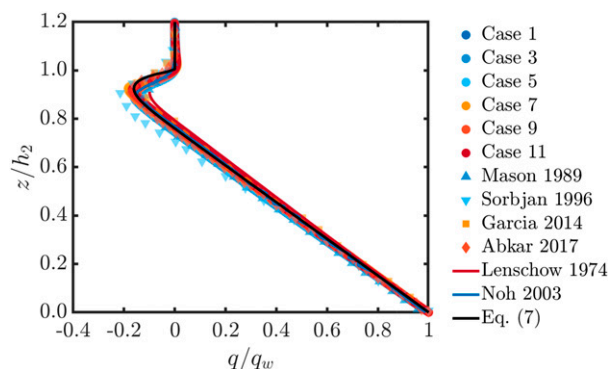


FIG. 3. Vertical profile of normalized potential temperature flux q/q_w . The data are shown as follows: circles, LES data (Table 1); up triangle, LES data of Mason (1989); down triangle, LES data of Sorbjan (1996); square, direct numerical simulations data of Garcia and Mellado (2014); diamond, LES data of Abkar and Moin (2017); red line, prediction given by Lenschow (1974); blue line, prediction given by Noh et al. (2003); black line, prediction given by Eq. (7) with $\epsilon = 0.044$ and $c_{II} = 1.32$. The figure shows that the proposed model captures the simulation trends very well.

b. Validation of analytical profiles

Figure 3 shows that with increasing height the normalized potential temperature flux profile q/q_w first decreases linearly from unity at the surface to a minimum at $z_i/h_2 = 1 - 2\epsilon$, before it rapidly increases to zero in the inversion layer ($1 - 2\epsilon \leq z/h_2 \leq 1$). The normalized thickness of the inversion layer, which is parameterized by ϵ , is expected to depend on the Richardson number (Deardorff et al. 1980), potential temperature gradient (Sorbjan 1996), and wind shear (Conzemius and Fedorovich 2006). However, we find that for the parameter range under consideration, the variation in the normalized thickness of the inversion layer is limited (see Table 1). Therefore, we use a fixed representative value $\epsilon = 0.044$ to model the potential temperature flux profile, and the figure

confirms that this ensures that the potential temperature flux profile obtained from the model agrees excellently with all available simulation data, which validates the chosen approach. To further confirm the validity of the potential temperature flux profile, we also compare our results in Fig. 3 with previous LES from Mason (1989), Sorbjan (1996), and Abkar and Moin (2017), the direct numerical simulations data by Garcia and Mellado (2014), and the empirical models by Lenschow (1974) and Noh et al. (2003). Clearly, the model predictions agree well with these previous studies.

In Fig. 4a we compare the wind speed in the bulk of the mixed layer ($0.4 \leq z/h_2 \leq 0.6$) against the normalized Obukhov length $-L/z_0$ with results from Tong and Ding (2020). The figure shows that our simulations convincingly confirm the validity of the convective logarithmic friction law for the wind speed [Eq. (16) with $C = 1$] over a much wider range of $-L/z_0 \in [3.6 \times 10^2, 0.7 \times 10^5]$ than previously considered ($-L/z_0 \in [2.5 \times 10^2, 1.5 \times 10^3]$). To further confirm the convective logarithmic friction law, Fig. 4b shows the ratio of the predicted and simulated mixed-layer mean velocity scale $U_m^{\text{pred}}/U_m^{\text{LES}}$ against the normalized Obukhov length $-L/z_0$. The figure shows that the predicted value is within 5% of the simulation result for all considered cases.

In Fig. 5 we compare the vertical profile of the mean streamwise velocity U for four typical cases with different surface potential temperature flux and roughness length with the simulation results. The filled symbols are the present LES data, the dashed line is the theoretical prediction given by the MOST, and the solid line is the prediction given by Eq. (20) with $\epsilon = 0.044$. The figure shows that the MOST accurately captures the surface layer's wind profile (lowest 20% of the boundary layer). However, in the mixed layer, the prediction of the MOST deviates significantly from the LES data. In particular, the discrepancy from the MOST increases as the surface potential temperature flux q_w decreases (Figs. 5b,c) or the roughness length z_0 increases (Figs. 5a,d). Therefore, MOST is seldom used to specify wind profiles outside of the

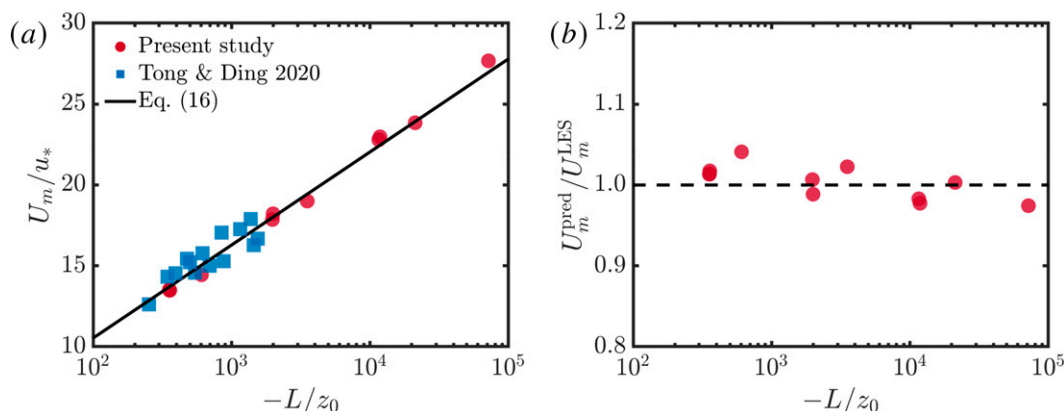


FIG. 4. The dependence of (a) the normalized mixed-layer mean velocity scale U_m/u_* and (b) the ratio of the predicted and simulated mixed-layer mean velocity scale $U_m^{\text{pred}}/U_m^{\text{LES}}$ against the normalized Obukhov length $-L/z_0$. The data are shown as follows: circles, LES data (Table 1); squares, LES data of Tong and Ding (2020); solid line, prediction given by Eq. (16) with $C = 1$ determined using a fit to the present simulation data.

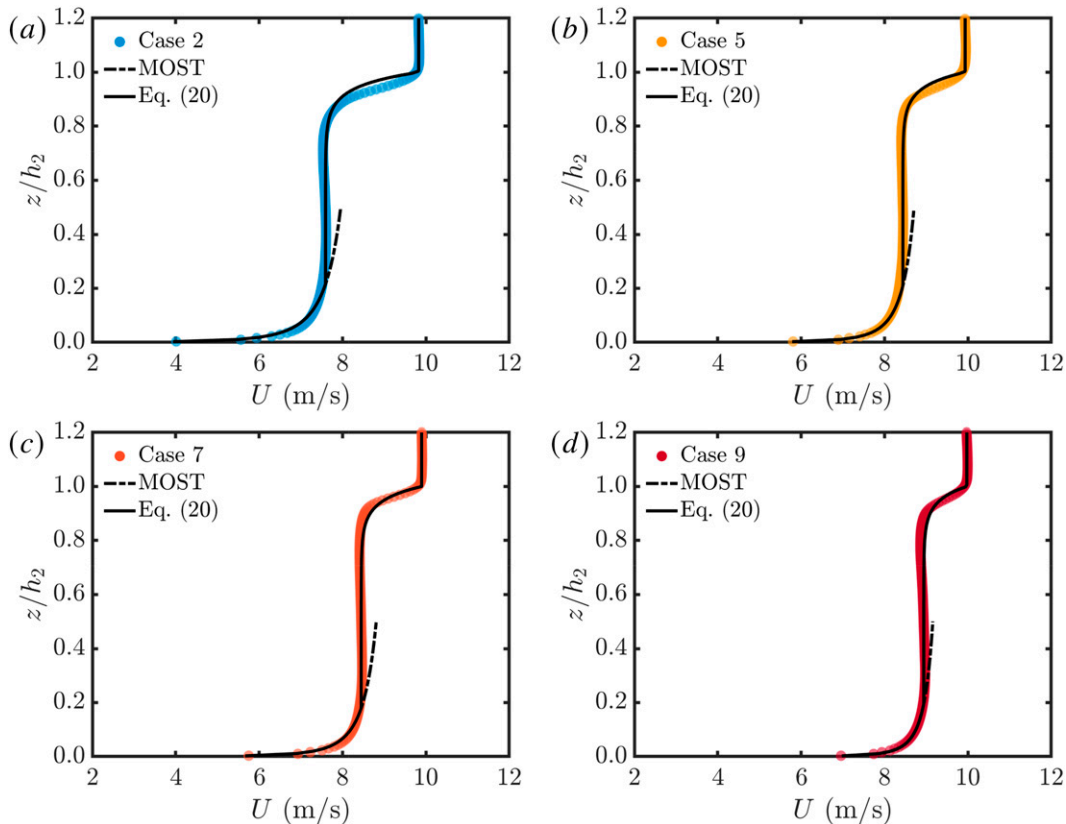


FIG. 5. Vertical profile of the mean streamwise velocity U . The data are shown as follows: filled circles, LES data (Table 1); dashed line, prediction given by the MOST; solid line, prediction given by Eq. (20) with $\epsilon = 0.044$. The prediction by the MOST is plotted outside the surface-layer region to demonstrate the difference with the new profile.

surface layer. Figure 5 shows that the proposed wind profile given by Eq. (20) accurately captures the velocity profile throughout the entire boundary layer. This excellent agreement confirms the validity of our proposed wind profile of Eq. (20) for atmospheric boundary layers in the range of studied parameters.

Figure 6 shows the corresponding profiles of the mean spanwise velocity V . The filled symbols are the present LES data and the solid line is the prediction given by Eq. (22) with $\epsilon = 0.044$. Overall, the agreement between the proposed wind profile given by Eq. (22) and the LES data is reasonably good in the entire boundary layer. This agreement confirms the validity of our proposed wind profile of Eq. (22) for CBLs in the range of studied parameters (i.e., $-L/z_0 \in [3.6 \times 10^2, 0.7 \times 10^5]$). We note that the figure confirms that the spanwise velocity V is much smaller than the streamwise velocity U . The figure also indicates that the magnitude of the geostrophic wind component $|V_g|$ increases as the surface potential temperature flux q_w decreases (Figs. 6b,c) or the roughness length z_0 increases (Figs. 6a,d).

4. Conclusions

This work uses a perturbation method approach in conjunction with the convective logarithmic friction law and

the Monin–Obukhov similarity theory to develop analytical expressions of the wind and potential temperature flux profiles in convective atmospheric boundary layers. The validity of the proposed wind [given by Eqs. (20) and (22)] and potential temperature flux profiles [given by Eq. (7)] has been confirmed by their excellent agreement with large-eddy simulations results for atmospheric boundary layers in the convective-roll dominant regime with $-z_i/L \gtrsim 10$, where L is the Obukhov length and z_i the inversion layer height. Furthermore, our simulations confirm that the convective logarithmic friction law of Eq. (16), which was originally proposed by Tong and Ding (2020) for the mixed-layer mean velocity scale, is valid for an extensive range of $-L/z_0$, namely, $-L/z_0 \in [3.6 \times 10^2, 0.7 \times 10^5]$, where z_0 is the surface roughness length. Since accurately capturing the coupling between meso- and microscale processes is a long-standing challenge in numerical weather predictions (Wyngaard 2004; Larsén et al. 2018; Veers et al. 2019), the proposed analytical profiles may be relevant for climate modeling and weather forecasting to better understand the effect of convective atmospheric boundary layers on, for example, wind farms. Possible future work will involve investigating models to predict the entrainment velocity at the top of CBLs and developing a high-order model that can capture the transition between the

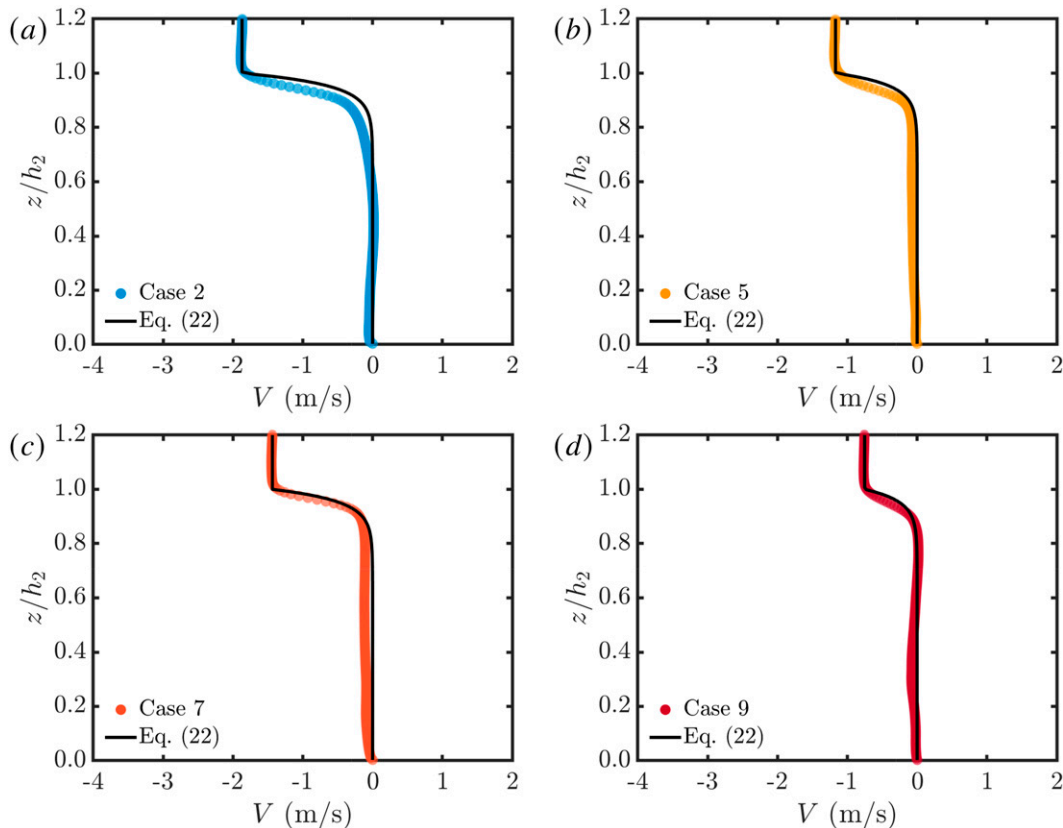


FIG. 6. Vertical profile of the mean spanwise velocity V . The data are shown as follows: filled circles, LES data (Table 1); solid line: prediction given by Eq. (22) with $\epsilon = 0.044$.

entrainment zone and free atmosphere. The latter may require a formal asymptotic series expansion of the governing equations, allowing for the separation into a time-dependent and steady-state problem at different orders.

Acknowledgments. This work was supported by the Hundred Talents Program of the Chinese Academy of Sciences, the National Natural Science Fund for Excellent Young Scientists Fund Program (Overseas), the National Natural Science Foundation of China Grant (11621202), the Shell–NWO/FOM initiative Computational sciences for energy research of Shell and Chemical Sciences, Earth and Life Sciences, Physical Sciences, Stichting voor Fundamenteel Onderzoek der Materie (FOM) and STW, and an STW VIDI Grant (14868). This work was sponsored by NWO Domain Science for the use of the national computer facilities. We acknowledge PRACE for awarding us access to Irene at Très Grand Centre de Calcul du CEA (TGCC) under PRACE Project 2019215098, and the advanced computing resources provided by the Supercomputing Center of the USTC.

Data availability statement. The data that support the findings of this study are available from the corresponding author upon reasonable request.

REFERENCES

- Abkar, M., and P. Moin, 2017: Large eddy simulation of thermally stratified atmospheric boundary layer flow using a minimum dissipation model. *Bound.-Layer Meteor.*, **165**, 405–419, <https://doi.org/10.1007/s10546-017-0288-4>.
- Albertson, J. D., 1996: Large eddy simulation of land-atmosphere interaction. Ph.D. thesis, University of California, Davis, 185 pp.
- , and M. B. Parlange, 1999: Surface length-scales and shear stress: Implications for land-atmosphere interaction over complex terrain. *Water Resour. Res.*, **35**, 2121–2132, <https://doi.org/10.1029/1999WR900094>.
- Arya, S. P. S., 1975: Comments on “Similarity theory for the planetary boundary layer of time-dependent height.” *J. Atmos. Sci.*, **32**, 839–840, [https://doi.org/10.1175/1520-0469\(1975\)032<0839:COTFTP>2.0.CO;2](https://doi.org/10.1175/1520-0469(1975)032<0839:COTFTP>2.0.CO;2).
- Blackadar, A. K., and H. Tennekes, 1968: Asymptotic similarity in neutral barotropic planetary boundary layers. *J. Atmos. Sci.*, **25**, 1015–1020, [https://doi.org/10.1175/1520-0469\(1968\)025<1015:ASINBP>2.0.CO;2](https://doi.org/10.1175/1520-0469(1968)025<1015:ASINBP>2.0.CO;2).
- Bou-Zeid, E., C. Meneveau, and M. Parlange, 2005: A scale-dependent Lagrangian dynamic model for large eddy simulation of complex turbulent flows. *Phys. Fluids*, **17**, 025105, <https://doi.org/10.1063/1.1839152>.
- Brutsaert, W., 1982: *Evaporation into the Atmosphere: Theory, History and Applications*. Springer, 312 pp.

- Businger, J. A., J. C. Wyngaard, Y. Izumi, and E. F. Bradley, 1971: Flux-profile relationships in the atmospheric surface layer. *J. Atmos. Sci.*, **28**, 181–189, [https://doi.org/10.1175/1520-0469\(1971\)028<0181:FPRITA>2.0.CO;2](https://doi.org/10.1175/1520-0469(1971)028<0181:FPRITA>2.0.CO;2).
- Calaf, M., C. Meneveau, and J. Meyers, 2010: Large eddy simulations of fully developed wind-turbine array boundary layers. *Phys. Fluids*, **22**, 015110, <https://doi.org/10.1063/1.3291077>.
- Cheng, Y., M. B. Parlange, and W. Brutsaert, 2005: Pathology of Monin-Obukhov similarity in the stable boundary layer. *J. Geophys. Res.*, **110**, D06101, <https://doi.org/10.1029/2004JD004923>.
- , Q. Li, D. Li, and P. Gentile, 2021: Logarithmic profile of temperature in sheared and unstably stratified atmospheric boundary layers. *Phys. Rev. Fluids*, **6**, 034606, <https://doi.org/10.1103/PhysRevFluids.6.034606>.
- Conzemius, R. J., and E. Fedorovich, 2006: Dynamics of sheared convective boundary layer entrainment. Part I: Methodological background and large-eddy simulations. *J. Atmos. Sci.*, **63**, 1151–1178, <https://doi.org/10.1175/JAS3691.1>.
- Deardorff, J. W., 1973: An explanation of anomalously large Reynolds stresses within the convective planetary boundary layer. *J. Atmos. Sci.*, **30**, 1070–1076, [https://doi.org/10.1175/1520-0469\(1973\)030<1070:AEOALR>2.0.CO;2](https://doi.org/10.1175/1520-0469(1973)030<1070:AEOALR>2.0.CO;2).
- , 1979: Prediction of convective mixed-layer entrainment for realistic capping inversion structure. *J. Atmos. Sci.*, **36**, 424–436, [https://doi.org/10.1175/1520-0469\(1979\)036<0424:POCMLE>2.0.CO;2](https://doi.org/10.1175/1520-0469(1979)036<0424:POCMLE>2.0.CO;2).
- , G. E. Willis, and B. H. Stockton, 1980: Laboratory studies of the entrainment zone of a convectively mixed layer. *J. Fluid Mech.*, **100**, 41–64, <https://doi.org/10.1017/S0022112080001000>.
- Ding, M., and C. Tong, 2021: Multi-point Monin–Obukhov similarity of turbulence cospectra in the convective atmospheric boundary layer. *Bound.-Layer Meteor.*, **178**, 185–199, <https://doi.org/10.1007/s10546-020-00571-4>.
- Dyer, A. J., 1974: A review of flux-profile relationships. *Bound.-Layer Meteor.*, **7**, 363–372, <https://doi.org/10.1007/BF00240838>.
- Gadde, S. N., A. Stieren, and R. J. A. M. Stevens, 2021: Large-eddy simulations of stratified atmospheric boundary layers: Comparison of different subgrid models. *Bound.-Layer Meteor.*, **178**, 363–382, <https://doi.org/10.1007/s10546-020-00570-5>.
- García, J. R., and J. P. Mellado, 2014: The two-layer structure of the entrainment zone in the convective boundary layer. *J. Atmos. Sci.*, **71**, 1935–1955, <https://doi.org/10.1175/JAS-D-13-0148.1>.
- Garratt, J. R., J. C. Wyngaard, and R. J. Francey, 1982: Winds in the atmospheric boundary layer—Prediction and observation. *J. Atmos. Sci.*, **39**, 1307–1316, [https://doi.org/10.1175/1520-0469\(1982\)039<1307:WITABL>2.0.CO;2](https://doi.org/10.1175/1520-0469(1982)039<1307:WITABL>2.0.CO;2).
- Haghsheenas, A., and J. P. Mellado, 2019: Characterization of wind-shear effects on entrainment in a convective boundary layer. *J. Fluid Mech.*, **858**, 145–183, <https://doi.org/10.1017/jfm.2018.761>.
- Holtslag, A. A. M., and C.-H. Moeng, 1991: Eddy diffusivity and countergradient transport in the convective atmospheric boundary layer. *J. Atmos. Sci.*, **48**, 1690–1698, [https://doi.org/10.1175/1520-0469\(1991\)048<1690:EDACTI>2.0.CO;2](https://doi.org/10.1175/1520-0469(1991)048<1690:EDACTI>2.0.CO;2).
- Hong, S.-Y., Y. Noh, and J. Dudhia, 2006: A new vertical diffusion package with an explicit treatment of entrainment processes. *Mon. Wea. Rev.*, **134**, 2318–2341, <https://doi.org/10.1175/MWR3199.1>.
- Johansson, C., A.-S. Smedman, U. Högström, J. G. Brasseur, and S. Khanna, 2001: Critical test of the validity of Monin–Obukhov similarity during convective conditions. *J. Atmos. Sci.*, **58**, 1549–1566, [https://doi.org/10.1175/1520-0469\(2001\)058<1549:CTOTVO>2.0.CO;2](https://doi.org/10.1175/1520-0469(2001)058<1549:CTOTVO>2.0.CO;2).
- Kaimal, J. C., J. C. Wyngaard, D. A. Haugen, O. R. Coté, Y. Izumi, S. J. Caughey, and C. J. Readings, 1976: Turbulence structure in the convective boundary layer. *J. Atmos. Sci.*, **33**, 2152–2169, [https://doi.org/10.1175/1520-0469\(1976\)033<2152:TSITCB>2.0.CO;2](https://doi.org/10.1175/1520-0469(1976)033<2152:TSITCB>2.0.CO;2).
- Katul, G. G., A. G. Konings, and A. Porporato, 2011: Mean velocity profile in a sheared and thermally stratified atmospheric boundary layer. *Phys. Rev. Lett.*, **107**, 268502, <https://doi.org/10.1103/PhysRevLett.107.268502>.
- Khanna, S., and J. G. Brasseur, 1997: Analysis of Monin–Obukhov similarity from large-eddy simulation. *J. Fluid Mech.*, **345**, 251–286, <https://doi.org/10.1017/S0022112097006277>.
- Larsén, X. G., E. L. Petersen, and S. E. Larsen, 2018: Variation of boundary-layer wind spectra with height. *Quart. J. Roy. Meteor. Soc.*, **144**, 2054–2066, <https://doi.org/10.1002/qj.3301>.
- LeMone, M. A., and Coauthors, 2019: 100 years of progress in boundary layer meteorology. *A Century of Progress in Atmospheric and Related Sciences: Celebrating the American Meteorological Society Centennial*, Meteor. Monogr., No. 59, Amer. Meteor. Soc., <https://doi.org/10.1175/AMSMONOGRAPHS-D-18-0013.1>.
- Lenschow, D. H., 1974: Model of the height variation of the turbulence kinetic energy budget in the unstable planetary boundary layer. *J. Atmos. Sci.*, **31**, 465–474, [https://doi.org/10.1175/1520-0469\(1974\)031<0465:MOTHVO>2.0.CO;2](https://doi.org/10.1175/1520-0469(1974)031<0465:MOTHVO>2.0.CO;2).
- Li, Q., Y. Cheng, and P. Gentile, 2021: Connection between mass flux transport and eddy diffusivity in convective atmospheric boundary layers. *Geophys. Res. Lett.*, **48**, e2020GL092073, <https://doi.org/10.1029/2020GL092073>.
- Lilly, D. K., 1968: Models of cloud-topped mixed layers under a strong inversion. *Quart. J. Roy. Meteor. Soc.*, **94**, 292–309, <https://doi.org/10.1002/qj.49709440106>.
- Liu, L., and R. J. A. M. Stevens, 2021: Effects of atmospheric stability on the performance of a wind turbine located behind a three-dimensional hill. *Renewable Energy*, **175**, 926–935, <https://doi.org/10.1016/j.renene.2021.05.035>.
- , S. N. Gadde, and R. J. A. M. Stevens, 2021a: Geostrophic drag law for conventionally neutral atmospheric boundary layers revisited. *Quart. J. Roy. Meteor. Soc.*, **147**, 847–857, <https://doi.org/10.1002/qj.3949>.
- , —, and —, 2021b: Universal wind profile for conventionally neutral atmospheric boundary layers. *Phys. Rev. Lett.*, **126**, 104502, <https://doi.org/10.1103/PhysRevLett.126.104502>.
- Mahrt, L., 1998: Nocturnal boundary-layer regimes. *Bound.-Layer Meteor.*, **88**, 255–278, <https://doi.org/10.1023/A:1001171313493>.
- Mason, P. J., 1989: Large-eddy simulation of the convective atmospheric boundary layer. *J. Atmos. Sci.*, **46**, 1492–1516, [https://doi.org/10.1175/1520-0469\(1989\)046<1492:LESOTC>2.0.CO;2](https://doi.org/10.1175/1520-0469(1989)046<1492:LESOTC>2.0.CO;2).
- McNaughton, K. G., R. J. Clement, and J. B. Moncrieff, 2007: Scaling properties of velocity and temperature spectra above the surface friction layer in a convective atmospheric boundary layer. *Nonlinear Processes Geophys.*, **14**, 257–271, <https://doi.org/10.5194/npg-14-257-2007>.
- Moeng, C.-H., 1984: A large-eddy simulation model for the study of planetary boundary-layer turbulence. *J. Atmos. Sci.*, **41**, 2052–2062, [https://doi.org/10.1175/1520-0469\(1984\)041<2052:ALESMT>2.0.CO;2](https://doi.org/10.1175/1520-0469(1984)041<2052:ALESMT>2.0.CO;2).
- , and P. P. Sullivan, 1994: A comparison of shear- and buoyancy-driven planetary boundary layer flows. *J. Atmos. Sci.*, **51**, 999–1022, [https://doi.org/10.1175/1520-0469\(1994\)051<0999:ACOSAB>2.0.CO;2](https://doi.org/10.1175/1520-0469(1994)051<0999:ACOSAB>2.0.CO;2).

- Monin, A. S., and A. M. Obukhov, 1954: Basic laws of turbulent mixing in the surface layer of the atmosphere. *Tr. Geofiz. Inst., Akad. Nauk SSSR*, **24**, 163–187.
- Nieuwstadt, F. T. M., J. Westerweel, and B. J. Boersma, 2016: *Turbulence: Introduction to Theory and Applications of Turbulent Flows*. Springer, 284 pp.
- Noh, Y., W. G. Cheon, S. Y. Hong, and S. Raasch, 2003: Improvement of the K-profile model for the planetary boundary layer based on large eddy simulation data. *Bound.-Layer Meteor.*, **107**, 401–427, <https://doi.org/10.1023/A:1022146015946>.
- Obukhov, A. M., 1946: Turbulence in an atmosphere with inhomogeneous temperature. *Tr. Inst. Teor. Geofiz. Akad. Nauk SSSR*, **1**, 95–115.
- Panofsky, H. A., H. Tennekes, D. H. Lenschow, and J. C. Wyngaard, 1977: The characteristics of turbulent velocity components in the surface layer under convective conditions. *Bound.-Layer Meteor.*, **11**, 355–361, <https://doi.org/10.1007/BF02186086>.
- Paulson, C. A., 1970: The mathematical representation of wind speed and temperature profiles in the unstable atmospheric surface layer. *J. Appl. Meteor.*, **9**, 857–861, [https://doi.org/10.1175/1520-0450\(1970\)009<0857:TMROWS>2.0.CO;2](https://doi.org/10.1175/1520-0450(1970)009<0857:TMROWS>2.0.CO;2).
- Rossby, C. G., and R. B. Montgomery, 1935: The layer of frictional influence in wind and ocean currents. *Papers in Physical Oceanography and Meteorology*, Vol. 3, No. 3, Massachusetts Institute of Technology and Woods Hole Oceanographic Institution, 101 pp.
- Salesky, S. T., and W. Anderson, 2020: Coherent structures modulate atmospheric surface layer flux-gradient relationships. *Phys. Rev. Lett.*, **125**, 124501, <https://doi.org/10.1103/PhysRevLett.125.124501>.
- , M. Chamecki, and E. Bou-Zeid, 2017: On the nature of the transition between roll and cellular organization in the convective boundary layer. *Bound.-Layer Meteor.*, **163**, 41–68, <https://doi.org/10.1007/s10546-016-0220-3>.
- Schröter, J. S., A. F. Moene, and A. A. M. Holtslag, 2013: Convective boundary layer wind dynamics and inertial oscillations: The influence of surface stress. *Quart. J. Roy. Meteor. Soc.*, **139**, 1694–1711, <https://doi.org/10.1002/qj.2069>.
- Siebesma, A. P., P. M. M. Soares, and J. Teixeira, 2007: A combined eddy-diffusivity mass-flux approach for the convective boundary layer. *J. Atmos. Sci.*, **64**, 1230–1248, <https://doi.org/10.1175/JAS3888.1>.
- Sorbján, Z., 1996: Effects caused by varying the strength of the capping inversion based on a large eddy simulation model of the shear-free convective boundary layer. *J. Atmos. Sci.*, **53**, 2015–2024, [https://doi.org/10.1175/1520-0469\(1996\)053<2015:ECBVT>2.0.CO;2](https://doi.org/10.1175/1520-0469(1996)053<2015:ECBVT>2.0.CO;2).
- Stoll, R., and F. Porté-Agel, 2008: Large-eddy simulation of the stable atmospheric boundary layer using dynamic models with different averaging schemes. *Bound.-Layer Meteor.*, **126**, 1–28, <https://doi.org/10.1007/s10546-007-9207-4>.
- Stull, R. B., 1976: The energetics of entrainment across a density interface. *J. Atmos. Sci.*, **33**, 1260–1267, [https://doi.org/10.1175/1520-0469\(1976\)033<1260:TEOEAD>2.0.CO;2](https://doi.org/10.1175/1520-0469(1976)033<1260:TEOEAD>2.0.CO;2).
- , 1988: *An Introduction to Boundary Layer Meteorology*. Kluwer Academic, 670 pp.
- Sullivan, P. P., and E. G. Patton, 2011: The effect of mesh resolution on convective boundary layer statistics and structures generated by large-eddy simulation. *J. Atmos. Sci.*, **68**, 2395–2415, <https://doi.org/10.1175/JAS-D-10-05010.1>.
- , C.-H. Moeng, B. Stevens, D. H. Lenschow, and S. D. Mayor, 1998: Structure of the entrainment zone capping the convective atmospheric boundary layer. *J. Atmos. Sci.*, **55**, 3042–3064, [https://doi.org/10.1175/1520-0469\(1998\)055<3042:SOTEZC>2.0.CO;2](https://doi.org/10.1175/1520-0469(1998)055<3042:SOTEZC>2.0.CO;2).
- Sun, J., and Y. Wang, 2008: Effect of the entrainment flux ratio on the relationship between entrainment rate and convective Richardson number. *Bound.-Layer Meteor.*, **126**, 237–247, <https://doi.org/10.1007/s10546-007-9231-4>.
- Tennekes, H., and J. L. Lumley, 1972: *A First Course in Turbulence*. MIT Press, 320 pp.
- , and A. G. M. Driedonks, 1981: Basic entrainment equations for the atmospheric boundary layer. *Bound.-Layer Meteor.*, **20**, 515–531, <https://doi.org/10.1007/BF00122299>.
- Tong, C., and M. Ding, 2020: Velocity-defect laws, log law and logarithmic friction law in the convective atmospheric boundary layer. *J. Fluid Mech.*, **883**, A36, <https://doi.org/10.1017/jfm.2019.898>.
- Troen, I. B., and L. Mahrt, 1986: A simple model of the atmospheric boundary layer; sensitivity to surface evaporation. *Bound.-Layer Meteor.*, **37**, 129–148, <https://doi.org/10.1007/BF00122760>.
- Veers, P., and Coauthors, 2019: Grand challenges in the science of wind energy. *Science*, **366**, eaau2027, <https://doi.org/10.1126/science.aau2027>.
- Wieringa, J., A. G. Davenport, C. S. B. Grimmond, and T. R. Oke, 2001: New revision of Davenport roughness classification. *Third European and African Conf. on Wind Engineering*, Eindhoven, Netherlands, Eindhoven University of Technology, 285–292, <https://pure.tue.nl/ws/portalfiles/portal/102902986/EACWE3.pdf>.
- Wu, Y.-T., and F. Porté-Agel, 2011: Large-eddy simulation of wind-turbine wakes: Evaluation of turbine parametrisations. *Bound.-Layer Meteor.*, **138**, 345–366, <https://doi.org/10.1007/s10546-010-9569-x>.
- Wyngaard, J. C., 2004: Toward numerical modeling in the “terra incognita.” *J. Atmos. Sci.*, **61**, 1816–1826, [https://doi.org/10.1175/1520-0469\(2004\)061<1816:TNMITT>2.0.CO;2](https://doi.org/10.1175/1520-0469(2004)061<1816:TNMITT>2.0.CO;2).
- , 2010: *Turbulence in the Atmosphere*. Cambridge University Press, 407 pp.
- Zhang, M., M. G. Arendshorst, and R. J. A. M. Stevens, 2019: Large eddy simulations of the effect of vertical staggering in extended wind farms. *Wind Energy*, **22**, 189–204, <https://doi.org/10.1002/we.2278>.
- Zilitinkevich, S. S., 1969: On the computation of the basic parameters of the interaction between the atmosphere and the ocean. *Tellus*, **21**, 17–24, <https://doi.org/10.1111/j.2153-3490.1969.tb00414.x>.
- , 1975: Resistance laws and prediction equations for the depth of the planetary boundary layer. *J. Atmos. Sci.*, **32**, 741–752, [https://doi.org/10.1175/1520-0469\(1975\)032<0741:RLAPEF>2.0.CO;2](https://doi.org/10.1175/1520-0469(1975)032<0741:RLAPEF>2.0.CO;2).
- , and J. W. Deardorff, 1974: Similarity theory for the planetary boundary layer of time-dependent height. *J. Atmos. Sci.*, **31**, 1449–1452, [https://doi.org/10.1175/1520-0469\(1974\)031<1449:STFTPB>2.0.CO;2](https://doi.org/10.1175/1520-0469(1974)031<1449:STFTPB>2.0.CO;2).
- , E. E. Fedorovich, and M. V. Shabalova, 1992: Numerical model of a non-steady atmospheric planetary boundary layer, based on similarity theory. *Bound.-Layer Meteor.*, **59**, 387–411, <https://doi.org/10.1007/BF02215460>.
- , S. A. Tyuryakov, Y. I. Troitskaya, and E. A. Mareev, 2012: Theoretical models of the height of the atmospheric boundary layer and turbulent entrainment at its upper boundary. *Izv. Atmos. Ocean. Phys.*, **48**, 133–142, <https://doi.org/10.1134/S0001433812010148>.